

# Performance Optimization and Characterization of 7-Pad Resistive PICOSEC Micromegas Detectors

A. Kallitsopoulou,<sup>a,1</sup> R. Aleksan<sup>a</sup> S. Aune<sup>b</sup> J. Bortfeldt<sup>d</sup> F. Brunbauer<sup>e</sup> M. Brunoldi<sup>f,g</sup> J. Datta<sup>h</sup> D. Desforge<sup>a</sup> G. Fanourakis<sup>i</sup> D. Fiorina<sup>f,g,2</sup> K. J. Floethner<sup>e,j</sup> M. Gallinaro<sup>k</sup> F. Garcia<sup>l</sup> I. Giomataris<sup>a</sup> K. Gnanvo<sup>m</sup> F.J. Iguaz<sup>a,3</sup> D. Janssens<sup>e</sup> F. Jeanneau<sup>a</sup> M. Kovacic<sup>n</sup> B. Kross<sup>m</sup> P. Legou<sup>a</sup> M. Lisowska<sup>e</sup> J. Liu<sup>o</sup> M. Lupberger<sup>j,p</sup> I. Maniatis<sup>b,c,4</sup> J. McKisson<sup>m</sup> Y. Meng<sup>o</sup> H. Muller<sup>e,p</sup> E. Oliveri<sup>e</sup> G. Orlandini<sup>e,q</sup> A. Pandey<sup>m</sup> T. Papaevangelou<sup>a</sup> M. Pomorski<sup>r</sup> E.F.Ribas<sup>a</sup> L. Ropelewski<sup>e</sup> D. Sampsonidis<sup>b,c</sup> L. Scharenberg<sup>e</sup> T. Schneider<sup>e</sup> E. Scorsone<sup>r</sup> L. Sohl<sup>b,5</sup> M. van Stenis<sup>e</sup> Y. Tsipolitis<sup>s</sup> S.E. Tzamarias<sup>b,c</sup> A. Utrobicic<sup>t</sup> I. Vai<sup>f,g</sup> R. Veenhof<sup>e</sup> P. Vitulo<sup>f,g</sup> X. Wang<sup>o</sup> S. White<sup>u</sup> W. Xi<sup>m</sup> Z. Zhang<sup>o</sup> Y. Zhou<sup>o</sup>

<sup>a</sup>IRFU, CEA-Université Paris-Saclay, F-91191 Gif-sur-Yvette, France

<sup>b</sup>Department of Physics, Aristotle University of Thessaloniki, GR-54124 Thessaloniki, Greece

<sup>c</sup>CIRI-AUTH, GR-57001 Thessaloniki, Greece

<sup>d</sup>Department for Medical Physics, Ludwig Maximilian University of Munich, 85748 Garching, Germany

<sup>e</sup>CERN, 1211 Geneva 23, Switzerland

<sup>f</sup>Dipartimento di Fisica, Università di Pavia, 27100 Pavia, Italy

<sup>g</sup>INFN Sezione di Pavia, 27100 Pavia, Italy

<sup>h</sup>Department of Physics and Astronomy, Stony Brook University, NY 11794-3800, USA

<sup>i</sup>Institute of Nuclear and Particle Physics, NCSR Demokritos, GR-15341 Agia Paraskevi, Attiki, Greece

<sup>j</sup>Helmholtz-Institut für Strahlen- und Kernphysik, University of Bonn, 53115 Bonn, Germany

<sup>k</sup>Laboratório de Instrumentação e Física Experimental de Partículas (LIP), Lisbon, Portugal

<sup>l</sup>Helsinki Institute of Physics, University of Helsinki, FI-00014 Helsinki, Finland

<sup>m</sup>Jefferson Lab, Newport News, VA 23606, USA

<sup>n</sup>Faculty of Electrical Engineering and Computing, University of Zagreb, 10000 Zagreb, Croatia

<sup>o</sup>State Key Laboratory of Particle Detection and Electronics, University of Science and Technology of China, 230026 Hefei, China

<sup>p</sup>Physikalisches Institut, University of Bonn, 53115 Bonn, Germany

<sup>q</sup>Friedrich-Alexander-Universität Erlangen-Nürnberg, 91054 Erlangen, Germany

<sup>r</sup>CEA-List, Diamond Sensors Laboratory, CEA-Saclay, F-91191 Gif-sur-Yvette, France

<sup>s</sup>National Technical University of Athens, Athens, Greece

<sup>t</sup>Ruder Bošković Institute, 10000 Zagreb, Croatia

<sup>u</sup>University of Virginia, Virginia, USA

E-mail: [alexandra.kallitsopoulou@cea.fr](mailto:alexandra.kallitsopoulou@cea.fr)

<sup>1</sup>Corresponding author

<sup>2</sup>Now at Gran Sasso Science Institute, Viale F. Crispi, 7 67100 L'Aquila, Italy

<sup>3</sup>Now at SOLEIL Synchrotron, L'Orme des Merisiers, 91190 Saint Aubin, France

<sup>4</sup>Now at Department of Particle Physics and Astronomy, Weizmann Institute of Science, Rehovot, Israel.

<sup>5</sup>Now at TUV NORD EnSys GmbH & Co. KG.

**ABSTRACT:** We present a comprehensive characterization of resistive PICOSEC Micromegas detector prototypes, tested under identical conditions—constant drift gap, field configurations, and photocathode—at the CERN SPS H4 beam line. This work provides a proof of concept for the use of resistive layer technology in gaseous timing detectors, demonstrating that robustness can be improved without compromising the excellent timing performance of PICOSEC Micromegas. Different resistive architectures and values were explored to optimize stability and ensure reliable long-term operation in challenging experimental environments. The prototype with a  $10\text{ M}\Omega$  resistive layer achieved the best overall performance, with a timing resolution of  $22.900 \pm 0.002\text{ ps}$  and a spatial resolution of  $1.190 \pm 0.003\text{ mm}$ , while charge sharing across multiple pads enabled combined timing resolutions below  $28\text{ ps}$ . A lower-resistivity ( $200\text{ k}\Omega$ ) configuration exhibited enhanced charge spread, leading to minor systematic offsets in reconstructed pad centers, yet maintained robust timing and spatial performance. Capacitive charge-sharing architectures improved spatial resolution in some regions but suffered from signal attenuation and nonuniform charge distributions, resulting in slightly degraded timing ( $33.300 \pm 0.002\text{ ps}$ ) and complex localization patterns. Mechanical precision, particularly readout planarity and photocathode alignment, was identified as critical for uniform detector response. These studies benchmark the potential of resistive layers for gaseous timing detectors and provide a foundation for scalable designs with optimized timing and spatial resolution across diverse experimental applications.

**KEYWORDS:** Gaseous detectors, Timing detectors, Micromegas, Resistive Detectors, Spatial Resolution, Multipad-Analysis

---

## Contents

|          |   |           |
|----------|---|-----------|
| <b>1</b> | <b>Introduction</b>   | <b>1</b>  |
| <b>2</b> | <b>The 7-pad Resistive Prototype Development</b>                    | <b>3</b>  |
| <b>3</b> | <b>Experimental Setup and Standard Waveform Analysis</b>            | <b>4</b>  |
| <b>4</b> | <b>Detector Alignment</b>   | <b>8</b>  |
| <b>5</b> | <b>Timing Characteristics of Individual Pads</b>                    | <b>12</b> |
| <b>6</b> | <b>Combined Timing and Spatial Information of the Full Detector</b> | <b>15</b> |
| <b>7</b> | <b>Conclusion and Discussion</b>                                    | <b>22</b> |

---

## 1 Introduction

The motivation for developing state-of-the-art detectors is to equip future experiments with high precision on time, energy, and position measurements. Among the many challenges faced by the field, precision timing stands out as a critical aspect of instrumentation technology. Accurate timing capabilities are essential for identifying the wide range of particles produced in environments characterized by high radiation flux and pile-up events. As modern facilities push toward increasingly intense particle beams and higher luminosities, the demand for detectors that can operate reliably under these conditions continues to grow [1].

The stringent requirements imposed by modern experiments push detector technologies to their operational limits. To meet the demands of high-luminosity environments, detectors must not only ensure excellent timing performance but also provide large-area coverage, resilience against aging effects, and the capability of multi-pad readout for precise tracking. In the domain of fast timing, solid-state detectors currently represent a benchmark technology [2]. However, promising alternatives are also emerging within the gaseous detector sector. Resistive Plate Chambers (RPCs), for instance, can achieve timing resolutions on the order of 30 ps [3, 4], while members of the MicroPattern Gaseous Detector (MPGD) family typically reach a few nanoseconds [4, 5]. Among them, Micromegas-based detectors stand out by combining competitive timing performance with additional advantages, such as scalability to large surfaces, cost-effectiveness, and high-rate capability.

The timing resolution of conventional Micromegas detectors is fundamentally limited by the diffusion of electrons within the large drift region and by the stochastic nature of ionization induced by the incident particle. These effects impose uncertainty on the conditions under which primary electrons are produced. The timing performance can be improved by suppressing the randomness

of ionization and ensuring that all primary electrons are produced at the same distance from the mesh.

We introduce the PICOSEC Micromegas Detector concept to address these limitations, as described in Fig. 1a. This novel Micromegas-based detection system is designed to achieve charge-particle timing with a precision of tens of picoseconds. Unlike conventional Micromegas detectors, where ionization occurs randomly within the gas volume, the PICOSEC configuration employs a Cherenkov radiator. When a relativistic charged particle traverses the radiator, Cherenkov photons are emitted. A thin photo-converting material converts these photons into photoelectrons, ensuring that the photoelectrons enter the gas volume simultaneously and at a uniform distance from the mesh.

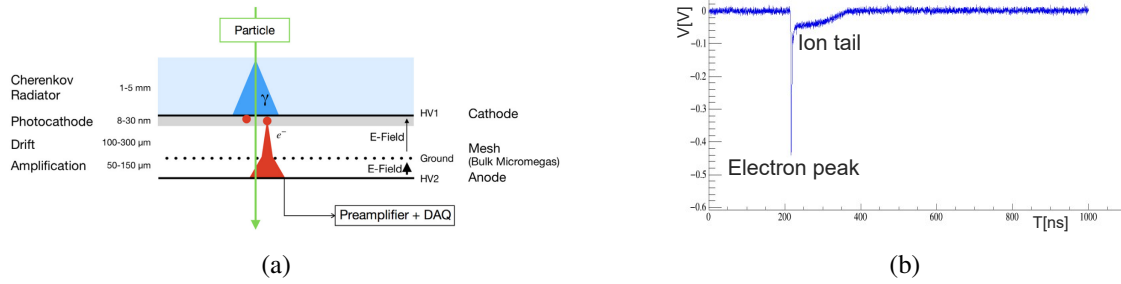


**Figure 1:** (a) Graphical representation of a PICOSEC Micromegas detector [6]. (b) Typical PICOSEC Micromegas signal after the amplifier.

The PICOSEC Micromegas detector operates as follows: a relativistic particle crossing the 3 mm thick  $\text{MgF}_2$  Cherenkov radiator emits photons, as its velocity exceeds the speed of light in the medium. These Cherenkov photons strike the photocathode, releasing photoelectrons in a highly synchronized way. When entering a gas volume under a strong electric field, the photoelectrons immediately trigger charge multiplication, forming an avalanche. As the avalanche reaches the micromesh, part of the charge passes through into the amplification gap, where a higher electric field induces further multiplication. This process generates a measurable current on the anode, which is recorded by the readout electronics. By this mechanism, the timing jitter—typically a few nanoseconds in conventional Micromegas—is reduced to the tens-of-picoseconds level, enabling much higher precision. An example of a PICOSEC Micromegas Signal can be found in Fig. 1b. This signal is composed of the fast (700 ps) electron peak and the slow (100 ns) ion tail components.

The key distinction from standard Micromegas lies in the reduced drift (or conversion) gap, which has been shrunk from 3 mm to 200  $\mu\text{m}$ . This smaller gap both suppresses direct ionization by incident particles and enhances the quantum efficiency of the photocathode. At the same time, the higher electric field in the drift region increases the Townsend coefficient, enabling the formation of early “preamplification avalanches”. These avalanches stabilize the multiplication process before charges undergo final amplification in the gap below the mesh [6].

The selection of an ideal gap is critical to ensuring the stability of preamplification avalanches, which directly correlates with improved timing resolution. A detailed study resulted in the fact that the avalanche formation drifts faster, with higher drift velocity, than its electron components, which means that the creation of the avalanche in the early stages of the drift gap will influence the timing

resolution of the detector [7]. These advantages are considered for the optimal operation of the PICOSEC Micromegas Detector.

Since the first proof-of-concept, the PICOSEC Micromegas detector has demonstrated remarkable progress in timing performance. The initial prototype, was a single channel of 1 cm diameter active zone operating in a gas mixture Ne : CF<sub>4</sub> : C<sub>2</sub>H<sub>6</sub> (80:10:10) at nominal temperature and pressure. It consisted of a 3 mm MgF<sub>2</sub> radiator window with 18 nm CsI semitransparent photocathode on top of a 5.5 nm Cr layer. This prototype achieved a record time resolution of 24 ps with 150 GeV/c muons, and a single-photoelectron resolution of 75 ps. Subsequent optimization, such as reducing the drift gap from 200  $\mu$ m to 120  $\mu$ m, improved the single-photoelectron resolution to 50 ps. Advancements on the design of the single channel prototypes, focusing on operation stability, respecting the signal integrity, noise reduction, and reassembly features, lead to pushing even further the timing resolution to 13.3 ps [8].

Building on these results, the collaboration has focused on extending the technology to larger active areas while maintaining stability, robustness, and uniform timing. A 100-channel detector with a 100 cm<sup>2</sup> active area, reached time resolutions of 17 ps in the central pad region and 17–18 ps over most of the surface, while the biggest 400-channel prototype with 400 cm<sup>2</sup> active area reached 25 ps with a uniformity of 33% [9, 10].

To develop more robust and modular prototypes that meet the demanding specifications of future applications, such as the ENUBET Project [11] or the Muon Collider [12], this work pursues several objectives. This work provides a proof of concept for the use of resistive layer technology in gaseous timing detectors, demonstrating that detector robustness can be improved without compromising the excellent timing resolution of PICOSEC Micromegas. As part of a broader R&D effort, different resistive architectures and values are explored to optimize stability and ensure reliable long-term operation in challenging experimental environments. Furthermore, for the first time, it explores the spatial resolution achievable with these technologies, assessing how the introduction of resistive layers impacts tracking capabilities. Together, these studies not only benchmark the potential of resistive layers for gaseous timing detectors but also lay the foundation for scalable designs tailored to diverse applications.

This paper is organized as follows. Section 2 introduces the seven-pad resistive Micromegas prototype used for all measurements. Section 3 describes the experimental setup and the standard waveform analysis procedure. Section 4 focuses on the detector alignment, while Section 5 presents the timing performance of the individual pads. Section 6 discusses the combined timing and spatial performance of the full detector assembly. Finally, Section 7 summarizes the main conclusions.

## 2 The 7-pad Resistive Prototype Development

To mitigate the destructive impact of discharges in the PICOSEC Micromegas detector, a resistive anode structure was implemented in the detector configuration. This approach efficiently quenches discharges, suppressing the streamer–spark transition while preserving high gain and stable operation under demanding conditions. The design, illustrated in Fig. 2, incorporates a thin Diamond-Like Carbon (DLC) resistive layer, electrically insulated from the pad electrodes by a 50  $\mu$ m polyimide layer and a 10  $\mu$ m adhesive layer.

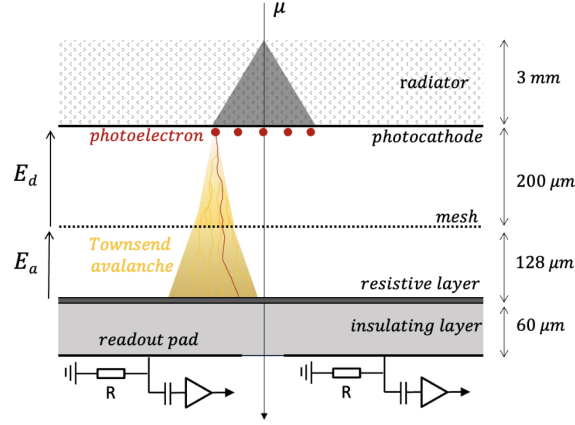


**Figure 2:** Schematic description of the resistive PICOSEC Micromegas detector layout [13].

All prototypes tested in this study were based on the same readout geometry, consisting of seven hexagonal pads with an outer diameter of 10 mm, an inner diameter of 8.6 mm, and an inter-pad spacing of about 200  $\mu\text{m}$  to reduce capacitive coupling and crosstalk. The resistive-layer contact and the mesh termination were routed outside the active area, to further reduce the probability of discharges in the sensitive region.

Within this common geometry, different resistive-layer implementations were investigated. Two surface resistivities were tested for the DLC films, 10  $\text{M}\Omega/\square$  and 200  $\text{k}\Omega/\square$ , chosen to represent extreme values in the relevant range. The first configuration employed a uniform DLC foil, in which a continuous resistive layer covered all pads, enabling charge dispersion and providing intrinsic protection against discharges. A second configuration, following a capacitive-sharing multilayer design, was tested, consisting of three stacked layers of hexagonal conductive pads separated by insulating films. The pad dimensions increased from 1.12 mm in the top layer to 5 mm in the bottom layer, arranged above the readout plane to enhance charge sharing and spatial resolution.

All prototypes were integrated into a common detector housing, illustrated in Fig. 3. The assembly procedure placed a copper drift spacer on the readout PCB, secured with screws to provide both electrical connection (via PCB traces and an SMA connector) and precise definition of the drift gap. A 5 cm diameter, 3 mm-thick  $\text{MgF}_2$  radiator, acting as the Cherenkov radiator and photocathode, was mounted on the spacer and held in place by a PEEK ring to ensure mechanical stability.

For comparison reasons, the prototypes were tested using an identical drift gap of 150  $\mu\text{m}$  to ensure compatibility. For assessing optimal timing performance, a standardized photocathode reference was employed, comprising an 18 nm CsI layer deposited on a 3.3 nm chromium (Cr) conductive substrate. A complete table with all the information about the prototypes developed and tested is given in Tab. 1.

### 3 Experimental Setup and Standard Waveform Analysis

The prototypes were tested during the 2023 RD51/DRD1 collaboration beam test campaigns at CERN. The measurements took place at the H4 beamline of the SPS using 150 GeV muons.

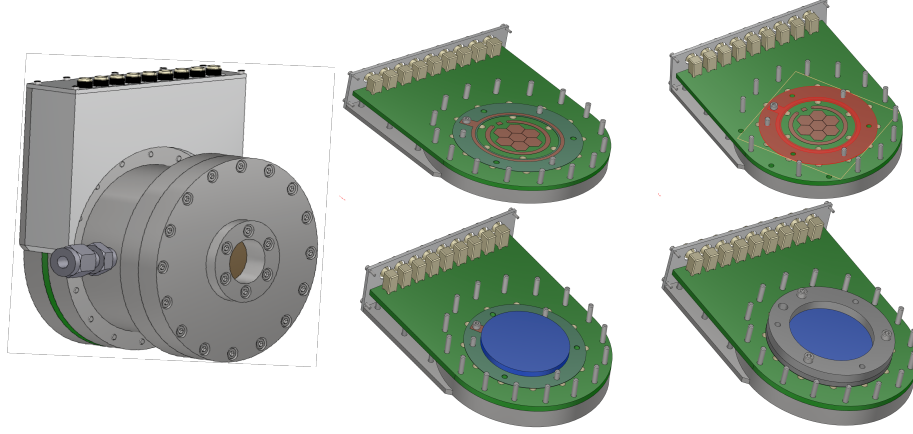


**Figure 3:** Left: Full detector assembly on the chamber. Right(from top to bottom): Step-by-step the assembly procedure, from the readout PCB, the drift copper ring, which preserves electrical contact and defines the drift gap size, the 5 cm crystal placement on top of the drift spacer, and the peak support.

**Table 1:** Summary of the tested configurations, showing key design parameters and common operating conditions.

| Resistivity            | Architecture / Layout  | Drift/Ampl. gap[ $\mu\text{m}$ ] | Photocathode           | Field configuration[kV/cm] |
|------------------------|--|----------------------------------|------------------------|----------------------------|
| 10 M $\Omega/\square$  | Continuous DLC plane (resistive foil)  | 150/128 $\mu\text{m}$            | 18 nm CsI on 3.3 nm Cr | 36.6/21.4                  |
| 200 k $\Omega/\square$ | Continuous DLC plane (resistive foil)  | 150/128 $\mu\text{m}$            | 18 nm CsI on 3.3 nm Cr | 36.6/21.4                  |
| 10 M $\Omega/\square$  | Three stacked hexagonal conductive layers: 1.12 mm (top), 2.5 mm (middle), 5 mm (bottom) | 150/128 $\mu\text{m}$            | 18 nm CsI on 3.3 nm Cr | 38/21.4                    |

As shown in Fig. 4, the experimental setup consisted of a beam telescope with up to six PICOSEC-Micromegas prototypes, a tracker made of three triple-GEM detectors, and an MCP-PMT<sup>1</sup> serving as precise timing references. The GEMs<sup>2</sup>, provided two-dimensional hit reconstruction, with signals digitized by the SRS system [14]. Particle tracks were reconstructed offline [15] using cluster

<sup>1</sup>Hamamatsu Microchannel plate photomultiplier tube (MCP-PMT) R3809U-50 [https://www.hamamatsu.com/jp/en/product/optical-sensors/pmt/pmt\\_tube-alone/mcp-pmt/R3809U-50.html](https://www.hamamatsu.com/jp/en/product/optical-sensors/pmt/pmt_tube-alone/mcp-pmt/R3809U-50.html)

<sup>2</sup>Gas mixture used was 70% Ar and 30% CO<sub>2</sub> at NTP.

analysis and linear fits, assuming straight trajectories due to the high beam momentum and absence of magnetic fields.

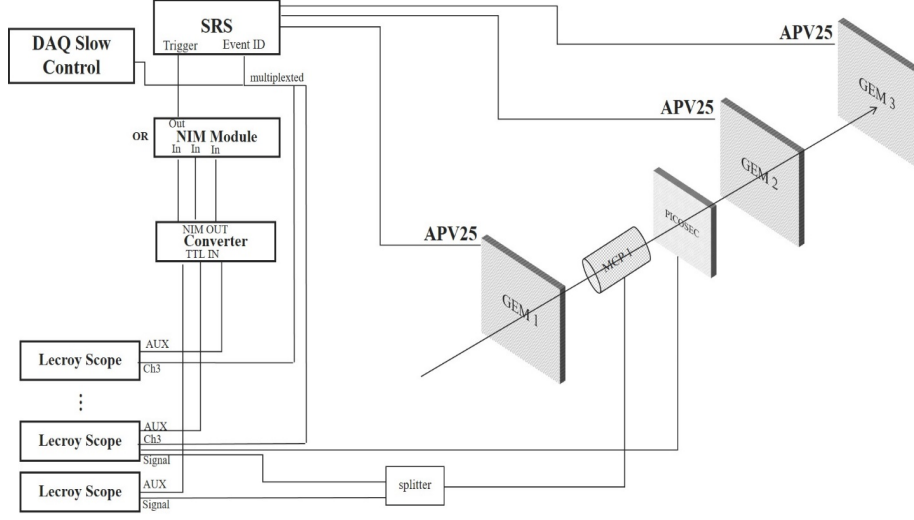


**Figure 4:** Block diagram and sketch of the electronic modules used to provide NIM signal to trigger the DAQ.

Trigger signals were derived from the MCP-PMTs and distributed to both the digitizers and the trigger logic of the SRS. As shown in Fig. 4, MCP signals were converted into NIM logic pulses and combined with an OR logic condition to provide a global trigger, synchronizing the tracker readout with the digitized PICOSEC-Micromegas waveforms. The APV25 data [14] were acquired with the DATE software<sup>3</sup>, while the waveforms from the prototypes were recorded with fast oscilloscopes. In offline analysis, the signals from the prototypes were matched to reconstructed particle trajectories, allowing for precise spatial and timing performance studies.

The signals from the seven PICOSEC-Micromegas pads pass through custom-made seven-channel board-structured preamplifiers. These amplifier cards are being used with a gain of 38 dB, a bandwidth of 650 MHz, and built-in discharge protection based on the RF amplifier design of [16]. PICOSEC-Micromegas signals are sampled with oscilloscopes from Lecroy Waverunner Series<sup>4</sup>, operating in 10 GS/s sampling rate.

The sampled waveforms, along with reference and trigger signals, were stored as binary files by the oscilloscope and processed using a dedicated analysis procedure.

The offline analysis followed a standardized workflow to ensure consistent signal reconstruction and timing extraction across all prototypes. The digitized waveforms from the PICOSEC-Micromegas detectors and the MCP-PMT reference were first pre-processed to correct for baseline fluctuations and suppress high-frequency noise. The baseline level was estimated from the pre-trigger region of each waveform and subtracted on an event-by-event basis. A three-point smoothing algorithm was then applied to reduce residual oscillations without distorting the pulse shape. This

<sup>3</sup>CERN. ALICE DAQ and ECS Manual (2010) <https://ph-dep-aid.web.cern.ch/ph-dep-aid/dateUserGuide/dateUserGuide.pdf>.

<sup>4</sup>Tedelyne LeCroy. Waverunner 8000 Series Datasheet (2018)



procedure ensures a robust and independent definition of the trigger point of the pulse boundaries, which is essential for extracting key parameters, such as the integrated charge [17].

The signal arrival time (SAT) was determined using a Constant Fraction Discrimination (CFD) technique based on a logistic fit to the leading edge of each pulse. The timing was extracted at 20% of the fitted amplitude, providing sub-sample precision and minimizing amplitude-dependent timing bias. The same method was applied to both the reference MCP-PMT and the detector under test. The SAT distribution was obtained by subtracting the PICOSEC-Micromegas timing from that of the MCP-PMT reference, both digitized by the same oscilloscope [6].

Although this approach is designed to avoid systematic effects, the observed correlation between the SAT and the signal amplitude arises from intrinsic detector physics. Specifically, the microscopic development of the avalanche introduces a dependence of the signal formation time on the initial photoelectron drift. As individual electrons drift slower than the propagating avalanche front, the time required to initiate the multiplication process manifests as an apparent time walk. This effect is unrelated to the analysis method itself but reflects the stochastic nature of avalanche formation. The dependence of SAT on signal amplitude was therefore parameterized and corrected offline. The corrected SAT distribution was then fitted with a Gaussian function, and the standard deviation of this fit represents the intrinsic timing resolution of the detector [7].

For a more accurate parameterization of this behavior, two observables can be considered: the electron-peak charge and the total charge of the waveform. The electron-peak charge is defined as the integral of a fitted function representing the fast component of the signal. Specifically, the electron peak, which begins at the triggering point and extends up to approximately 6 ns after the maximum amplitude, is fitted using a double-sigmoid function:

$$f(x; p_0, p_1, p_2, p_3, p_4, p_5) = p_3 + \frac{p_0}{1 + e^{-(x-p_1)p_2}} \times \frac{1}{1 + e^{-(x-p_4)p_5}} \quad (3.1)$$

where  $p_0$  and  $p_3$  are the maximum and minimum values of the amplitude,  $p_1$  is the steepness of the fitted function,  $p_2$  is the half point of the rise-time, and similarly,  $p_4$  and  $p_5$  are the steepness and the half point of the falling edge, respectively.

However, the total integrated charge was found to be a more robust and reliable observable, since determining the exact endpoint of the electron peak is often challenging. In particular, accurately identifying the transition between the electron peak and the onset of the ion tail can be difficult due to signal fluctuations. To address this, the endpoint of each waveform was determined using the cumulative sum of the waveform. Within a time window of 200 ns from the triggering point, the local minimum of the cumulative sum distribution was identified and used as the upper integration bound for total charge calculation [17].

Measuring the timing performance of large-area detectors poses a challenge when selecting a reference device, which must provide both superior resolution and spatial uniformity compared to the detector under test. Although large-area MCP-PMTs are available, their Signal Arrival Time uniformity must be well understood to avoid introducing biases. Previous studies [18] showed that the MCP-PMT time resolution is below 6 ps at the center but deteriorates rapidly toward the edges. To mitigate this effect, only the central region of the MCP was used in the present measurements.

For those measurements, the MCP was mounted on a movable stage and scanned over the detector area in a  $20 \times 20 \text{ mm}^2$  grid with 2.5 mm steps, ensuring about 75% overlap. By setting a

sufficiently high threshold, events from the outer regions were excluded, and uniform data collection was achieved through synchronization with the number of recorded events. The data used in this work, are collected during long runs, more than 500,000 triggers were collected with the detectors operated under stable operation, with the field configurations described in Tab. 1.

#### 4 Detector Alignment

To accurately study the timing performance of the multi-pad PICOSEC-Micromegas prototypes, as mentioned in [19], it is essential to determine the precise position of each readout pad with respect to the global tracking reference. This alignment ensures that charge sharing and timing correlations between neighboring pads are correctly interpreted in the beam reference frame. The same method was used for all the different prototypes tested, but for simplicity, we describe in detail using the data recorded by the central pad of the  $10\text{ M}\Omega/\square$  prototype.

To accurately study the timing performance of the multi-pad PICOSEC-Micromegas prototypes, it is essential to determine the precise position of each readout pad with respect to the global tracking reference. This alignment ensures that charge sharing and timing correlations between neighboring pads are correctly interpreted in the beam reference frame.

The procedure begins with the alignment of each detector and pad to the tracking system, using the trajectories reconstructed by the GEM telescope. For every pad, a two-dimensional map of the average total charge is constructed by correlating the reconstructed track impact positions with the measured charge on that pad. Since the beam uniformly illuminates the active area, the charge-weighted mean positions provide an unbiased first estimate of each pad center.

A refined determination of the pad centers is achieved through a multistage algorithm that combines binning, charge filtering, and charge-weighted fitting. The active area of the pad plane is divided into uniform bins of  $0.5\text{ mm} \times 0.5\text{ mm}$ , and for each bin the number of reconstructed tracks and the total collected charge are computed. The number of tracks per bin, representing the charge entries in each 2D bin, and the charge-weighted histogram, representing the sum of deposited charges in each bin for the corresponding central pad of the detector, are shown in Fig. 5. From these quantities, the bin-averaged charge

$$\bar{Q}_{xy} = \frac{\sum_i q_i}{N_i}$$

is calculated, where  $q_i$  represents the charge associated with each track segment and  $N_i$  the number of entries in the bin.

To suppress the impact of statistical noise, only bins fulfilling basic quality conditions are retained: a minimum number of tracks ( $T_{\min} = 20$  by default) and a minimum average charge ( $Q_{\min} = 4\text{ pC}$ ). This filtering isolates the physically relevant signal region while excluding bins dominated by noise or edge effects.

The filtered two-dimensional charge distribution is then projected along the  $x$  and  $y$  axes to obtain one-dimensional charge profiles,  $\bar{Q}_x(x_i)$  and  $\bar{Q}_y(y_j)$ . These distributions are expected to be approximately symmetric around the pad center, as shown in Fig. 6. To determine the precise centroid, each profile is fitted with a symmetric second-order polynomial of the form

$$f(x) = a(x - x_0)^2 + b,$$

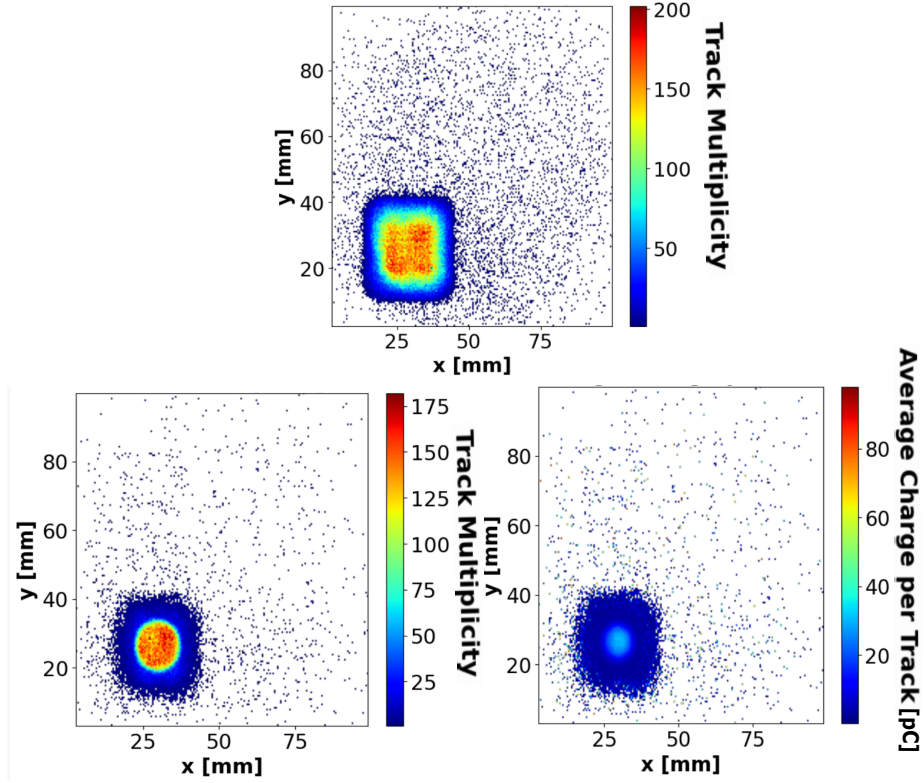


**Figure 5:** Top: 2D distribution of the beam profile that illuminates the area around the instrumented PICOSEC-Micromegas detector. Bottom: (Left) Track hits, representing the number of entries in each 2D bin. (Right) 2D track distribution weighted by pad-0 charge.

where  $x_0$  (and analogously  $y_0$ ) corresponds to the position of the maximum charge density, this value represents the charge-weighted centroid of the pad response function, which we interpret as the pad's geometric center in the beam reference frame.

Each fit is weighted by the statistical uncertainty of the charge in each bin,  $\sigma_{\bar{Q}} = \bar{Q}/\sqrt{N_{\text{tracks}}}$ , ensuring that bins with higher statistics dominate the fit. The covariance matrix from the polynomial fit provides the uncertainty on the extracted center coordinates, typically at the level of a few tens of micrometers.

This procedure yields a robust and data-driven estimate of the pad centers and their relative alignment within the detector plane. The final coordinates, expressed in the global beam frame, are used as reference positions for subsequent timing and spatial correlation analyses across pads.

Accurate spatial reconstruction of charged-particle hits within the detector plane requires that the geometrical model of the detector be aligned with the measured positions of its readout pads. Small mechanical tolerances, mounting deviations, or rotations between the physical detector and the global beam frame can lead to systematic offsets if not properly corrected. This section details the alignment and angular calibration procedure, which enables the transformation from the experimental pad coordinates to a normalized local detector frame suitable for charge-sharing and timing analyses.

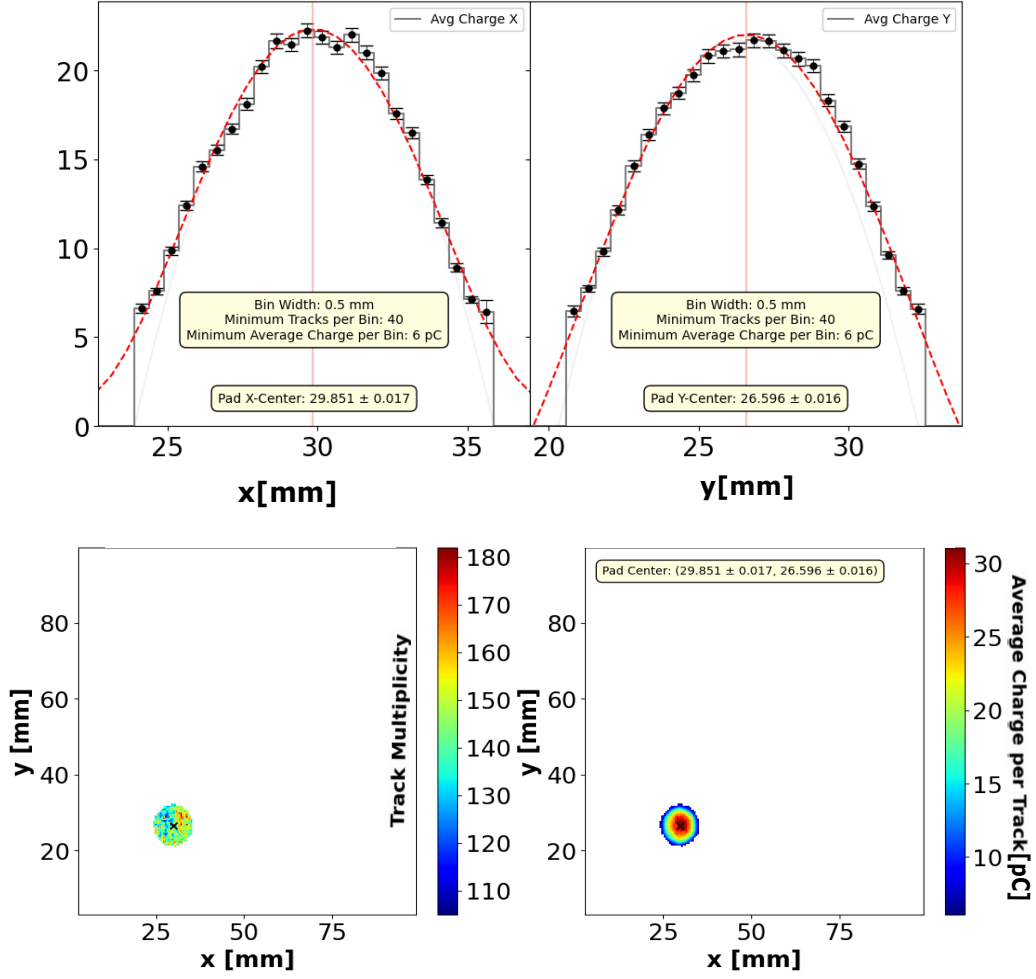


**Figure 6:** Top: X and Y projections of the average charge distribution of pad-0. The dashed red line corresponds to a second-order even polynomial that fits the symmetric distribution, and gives the  $x_c, y_c$  information. Bottom: The filtered 2D distributions for tracks and average charge on the pad-0 position.

The detector is modeled as a regular array of hexagonal pads, each representing an independent readout element. This geometry is implemented computationally in the HexDetector class, which constructs the hexagonal lattice by recursively placing neighboring pads at fixed angular offsets of  $60^\circ$ . Each pad is characterized by its inner radius  $r_{\text{inner}} = 4.3$  mm, defining the distance from the pad center to the midpoint of one edge. The corresponding outer radius is given by  $r_{\text{outer}} = \frac{2}{\sqrt{3}}r_{\text{inner}} = 4.97$  mm.

The distance between the centers of adjacent pads is therefore:

- $2r_{\text{inner}} = 8.6$  mm along horizontal axes, and
- $r_{\text{inner}}\sqrt{3} = 7.45$  mm along diagonal axes at  $\pm 60^\circ$ .

A 7-pad configuration is initialized by placing the central pad at the origin (0, 0) in local coordinates, and its six neighbors at the prescribed hexagonal offsets. The measured pad centers from calibration are then imported as  $(x_i^{meas}, y_i^{meas})$ , forming the experimental reference for the alignment.

To determine the global translation and rotation between the physical detector and the idealized model, a non-linear least-squares minimization is performed. The objective function is defined as:

$$\chi^2(x, y, \theta) = \sum_{i=1}^7 \left[ \left( \frac{x_i^{meas} - x_i^{det}(x, y, \theta)}{\sigma_{x_i}} \right)^2 + \left( \frac{y_i^{meas} - y_i^{det}(x, y, \theta)}{\sigma_{y_i}} \right)^2 \right], \quad (4.1)$$

where  $(x_i^{det}(x, y, \theta), y_i^{det}(x, y, \theta))$  are the detector model predictions after applying a translation  $(x, y)$  and rotation  $\theta$ . The initial guesses for  $(x, y, \theta)$  are derived from approximate detector placement measurements. The minimization is carried out using the `scipy.optimize.minimize` function with bounded parameters to ensure physical realism ( $|x|, |y| < 15$  mm,  $|\theta| < 0.2$  rad).

The best-fit parameters  $(x^*, y^*, \theta^*)$  correspond to the global transformation that minimizes the residuals between measured and modeled pad centers. In the case of the  $10 \text{ M}\Omega/\square$ , as shown in Fig.7, the resulting rotation angle was  $\theta^* = 5.5^\circ$ . This correction compensates for the slight tilt of the detector relative to the beam reference frame.

### Application of the Angular Correction

After obtaining the optimal transformation parameters, all measured track and hit positions are mapped into the detector's local coordinate system. Each point  $(x, y)$  is first translated so that the rotation center coincides with the geometric center of the detector:

$$x' = x - x_{center}, \quad (4.2)$$

$$y' = y - y_{center}. \quad (4.3)$$

The translated coordinates  $(x', y')$  are then rotated by the best-fit angle  $\theta^*$  using the standard 2D rotation matrix:

$$x_{rot} = \cos \theta^* \cdot x' - \sin \theta^* \cdot y', \quad (4.4)$$

$$y_{rot} = \sin \theta^* \cdot x' + \cos \theta^* \cdot y'. \quad (4.5)$$

The transformed dataset  $(x_{rot}, y_{rot})$  defines a normalized local coordinate system in which the pad centers coincide with the idealized hexagonal geometry. This alignment ensures that the subsequent timing and signal reconstruction analyses are free from geometric distortions caused by angular misalignment.

All steps of the procedure are fully reproducible using the provided `HexDetector` class and the corresponding alignment script in Python. The method ensures that the geometrical model of the detector matches the measured pad layout with sub-millimeter accuracy, sufficient for the subsequent timing and signal reconstruction analyses.

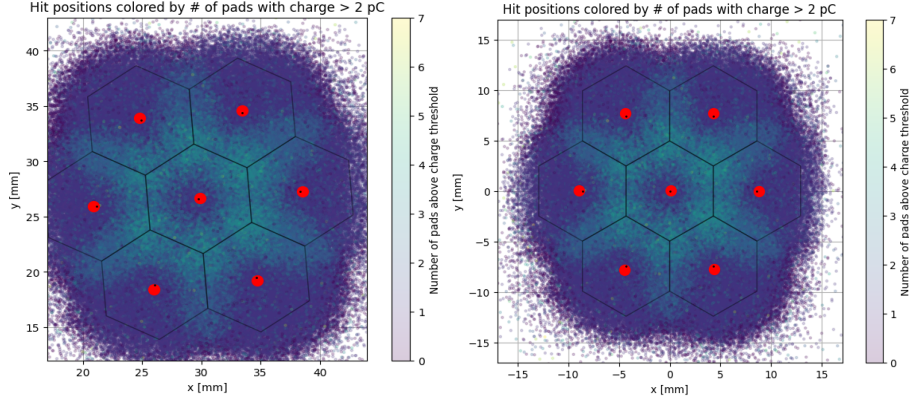


**Figure 7:** (Left) Tracks as shown in global beam frame. (Right) Tracks as shown in the local symmetric frame, where tracks are rotated to  $5.5^\circ$ . With red circles, the reconstructed pad centers are based on the charge-weighted track hit positions on the detector plane. With black dots, the expected geometrical pad centers.

## 5 Timing Characteristics of Individual Pads

To ensure that the derived timing properties of each pad reflect the intrinsic response of the detector and not artifacts of the data acquisition or geometry, several quality cuts were introduced. The raw pulse amplitudes were first inspected to identify saturation effects arising from the dynamic range limit of the oscilloscope digitizer. This selection removes high-amplitude events where the signal was cut by the digitizer, improving the consistency of the CFD time extraction.

The reconstructed track parameters, provided by the external triple-GEM telescope, were used to ensure that only well-defined particle trajectories were associated with valid PICOSEC events. The  $\chi^2$  value from the telescope track fit was used as a measure of the track quality. Events with  $\chi^2 > 3$  were rejected, corresponding to about 7% of the total statistics. This cut eliminates poorly reconstructed tracks that could lead to mismatched hit positions and hence deterioration of the pad center estimation.

To minimize the contribution of induced signals on neighboring pads, through the resistive layer, only events reconstructed within the active radius of each pad were considered. Based on the hexagonal pad geometry, the fiducial area was defined as a circular region of radius  $r < 5$  mm around the pad center. This selection ensures that the waveform corresponds to a direct local response rather than a resistive or capacitive coupling from adjacent electrodes.

Following the timing analysis procedure described previously, based on the Constant Fraction Discrimination (CFD) method, we extracted the SAT for each pad and investigated its dependence on the total charge. Several parameterization approaches were tested to describe the mean SAT as a function of charge, including Gaussian fitting and median-based extraction per charge bin [17]. Both methods yielded consistent results, and the Gaussian mean was adopted as the standard estimator.

The dependence of the SAT on total charge,  $\text{SAT}(q)$ , was modeled using a double-exponential function plus a constant term, as expressed by:

$$f(q; p_0, p_1, p_2, p_3, p_4) = e^{(p_0 q + p_1)} + e^{(p_2 q + p_3)} + p_4 \quad (5.1)$$



This parameterization captures the characteristic trend of the time-walk effect across the charge spectrum. The systematic dependence of SAT on signal amplitude was then corrected by subtracting the fitted function  $f(q)$  from the measured data points on an event-by-event basis, yielding the corrected SAT distributions. The same correction approach was used to parameterize the timing resolution, obtained from the RMS of the SAT distributions, as a function of total charge. Both fits are represented as the red dashed lines of Fig. 8.

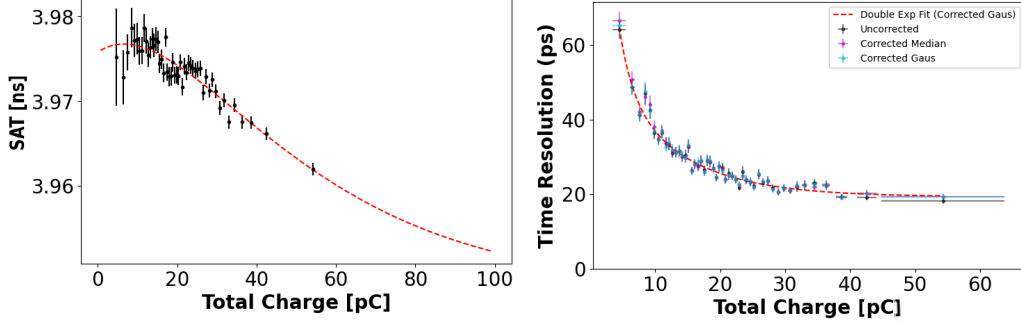


**Figure 8:** (Left) Dependence of SAT versus total charge, after the applied cuts, for saturation,  $\chi^2$ , and fiducial cut at radial distance of 5 cm and with their double exponential fit function distribution. (Right) Timing Resolution as a function of Total Charge for the pad-0 region of the 7-pad detector. With black, the raw values, and with magenta and cyan, the corrected values based on their SAT correction.

After the application of all quality and geometrical cuts, the corrected SAT and timing resolution were examined for distinct regions of each pad, defined by concentric radial zones with respect to the reconstructed pad center. Three radial regions were considered: 0–2.5 mm, 2.5–5 mm, and 5–7.5 mm. The results demonstrated that central regions exhibit superior timing performance, with a timing resolution of  $\sigma = 22.900 \pm 0.0002$  ps, Fig.9, while the timing resolution gradually degrades toward the outer regions of the pad.

Finally, to investigate spatial variations in timing performance across the entire pad surface, a dedicated ring-scan analysis was performed. The pad area was divided into concentric rings corresponding to the same radial intervals. For each ring, the corrected SAT distribution was fitted with a Gaussian to extract the local timing resolution. These values were then mapped spatially by performing a two-dimensional circular scan over the pad plane, using overlapping circular regions of 2 mm radius centered on a Cartesian grid of positions in the local pad frame. The resulting timing resolution heatmap provides a comprehensive view of the spatial homogeneity and confirms the internal consistency of the applied time-walk corrections, as it can be seen in Fig.10. The timing resolution is consistently below 30 ps over the 10 mm active area of a single cell.

Up to this point, the analysis has focused on the timing performance of individual pads, where the timing information was derived from a single pad per event. This approach is adequate when the impact point of a minimum ionizing particle (MIP) lies close to the pad center, such that the Cherenkov cone is contained entirely within that pad and most of the avalanching electrons are collected there. However, for a large-area detector, the impact point of most MIPs will be closer to the junction between neighboring pads than their center. In such cases, the induced signal is shared

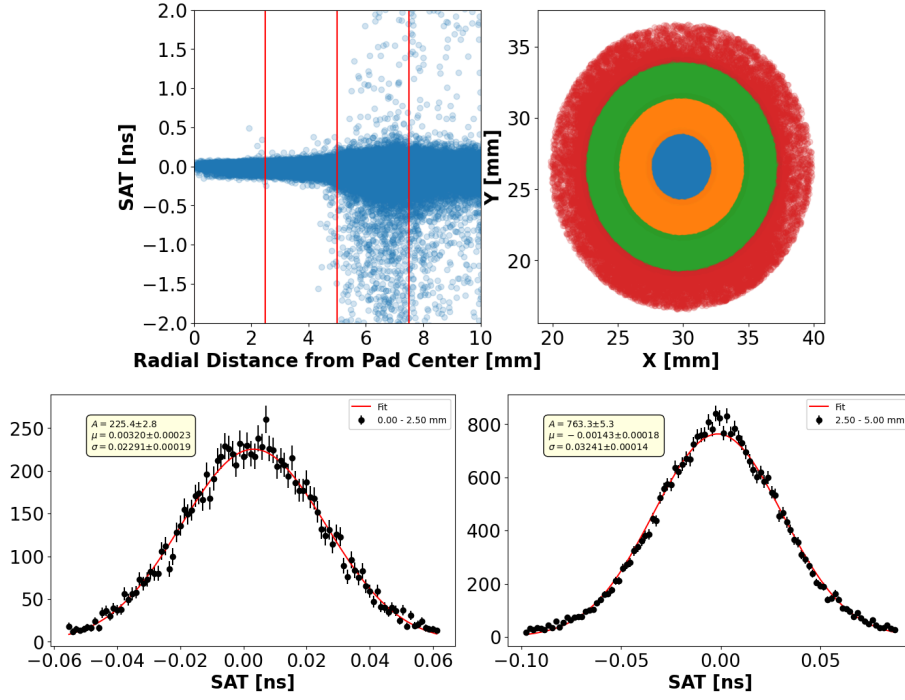


**Figure 9:** (Top) 2D graph of the corrected SAT distribution, divided into four rings: [0, 2.5] mm , [2.5, 5] mm , [5, 7.5] mm and [7.5, 10] mm. (Bottom) Corrected timing resolution in the respective concentric rings, [0, 2.5] mm, [2.5, 5] mm, red lines correspond to Gaussian fits.

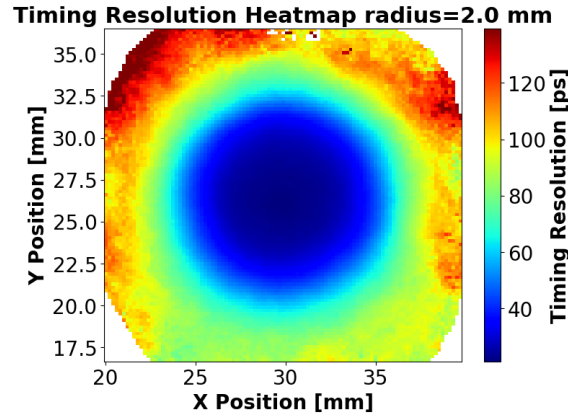


**Figure 10:** 2D circular scan producing timing heatmap for the pad-0 region.

among multiple pads, each providing an independent measurement of the SAT. For completeness, Fig.11 shows the dependence of SAT on total charge for all seven pads of the detector. To enable direct comparison across pads, the cable delays were subtracted from the SAT values, ensuring a consistent reference for visualizing the pad-to-pad variations.



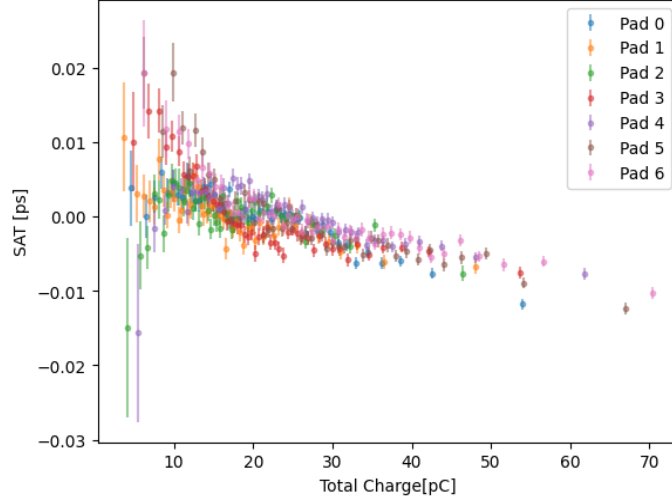


**Figure 11:** Dependence of SAT versus total charge for all the pads of the 10 MΩ prototype. The SAT values are not corrected for time-walk; just the mean values have been subtracted for better visualization.

## 6 Combined Timing and Spatial Information of the Full Detector

To develop a truly stand-alone detector capable of precise timing over large areas, the timing reconstruction must be performed independently of any external spatial information. Relying on an external tracking system would contradict this objective, as it would introduce external spatial constraints. The analysis conducted so far relies exclusively on the total waveform charge measured by each PICOSEC-Micromegas pad, showing that the timing resolution can be fully parameterized as a function of the collected charge. Before proceeding further and setting aside the use of tracking data, it is essential to assess the detector’s intrinsic spatial reconstruction capability.

### First Indications of Spatial Resolution Studies

The spatial resolution of the 7-pad prototype is therefore evaluated using a method that exploits the charge-sharing pattern among neighboring pads to reconstruct the impact position of the incident particles.

For each event, the total collected charge per pad and its corresponding SRS event number are used to merge the per-pad data into a unified structure. The initial event coordinates are estimated as the mean of the recorded hit positions over all pads participating in the event:

$$\bar{x} = \frac{1}{N} \sum_i hit X_i, \quad (6.1)$$

$$\bar{y} = \frac{1}{N} \sum_i hit Y_i \quad (6.2)$$

where  $N$  is the number of pads registering a signal in the same event.

A fiducial selection is applied to ensure that reconstructed hits lie within the central region of the detector, reducing edge effects that may distort charge interpolation. The selected region corresponds to a radial distance of  $r_{center} < 7.5$  mm from the detector's geometric center, as shown in Fig. 12.

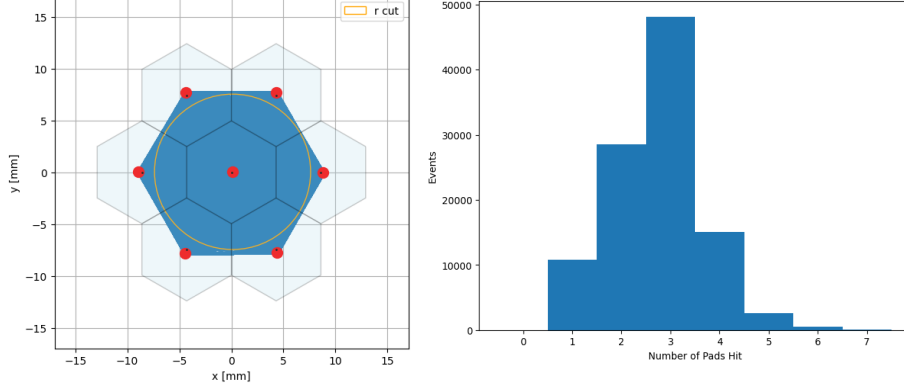


**Figure 12:** (Left) Reconstructed hit positions overlaid on the pad layout with coloring by multiplicity. (Right) Histogram of  $N_{hits}$  across all the events, with median at three active pads.

To reconstruct the hit position, we perform a charge-weighted interpolation over the pad centers:

$$x_{reco} = \frac{\sum_i Q_i x_i}{\sum_i Q_i}, \quad (6.3)$$

$$y_{reco} = \frac{\sum_i Q_i y_i}{\sum_i Q_i} \quad (6.4)$$

where  $Q_i$  is the total charge recorded on pad  $i$ , and  $(x_i, y_i)$  are the pad center coordinates. Pads with no signal contribute zero weight.

The reconstructed hit positions  $(x_{reco}, y_{reco})$  are compared to the averaged reference coordinates  $(\bar{x}, \bar{y})$ , and the residuals  $(\delta x, \delta y)$  are computed to evaluate the spatial resolution. Both residual distributions are fitted with a Gaussian function, yielding a spatial precision of  $1.19 \pm 0.003$  mm in both X and Y directions, as shown in Fig. 13. The values were extracted from Gaussian fits to the overall residual distributions, which represent the superposition of multiple event subsets corresponding to all different pad multiplicities, ranging from single-pad fits to events involving all seven active pads.

Fig. 14 shows that after repeating the same procedure for different pad multiplicities, the best performance is achieved for events involving three active pads, balancing information from charge sharing with minimal charge dilution effects.

### Combination of Timing Information Across the Detector Area

A key objective of this study is to maintain the independence of the applied timing analysis from spatial information, even in events where the Cherenkov cone is shared among multiple pads. In such cases, several pads are activated simultaneously, each recording an independent measurement

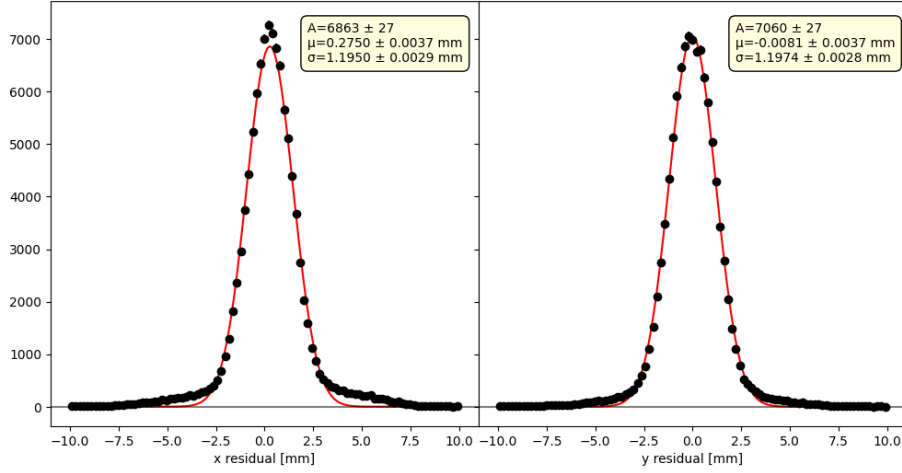


**Figure 13:** The spatial residuals for X and Y, respectively, fitted with a Gaussian function (red line) corresponding to  $1.19 \pm 0.003$  mm both in X and Y direction, spatial resolution. The error bars are too small to be observed for number of pads below 6.

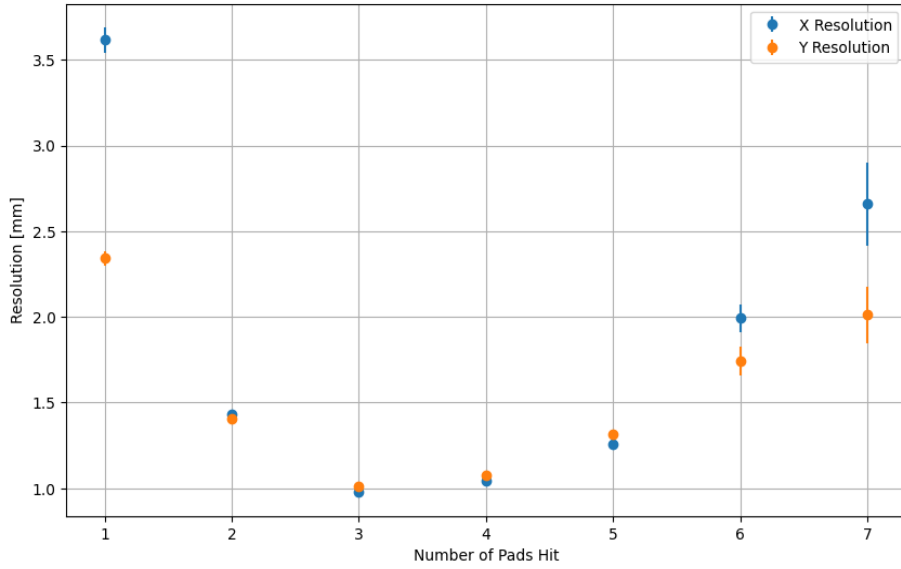


**Figure 14:** Spatial resolution versus  $N_{hits}$ . The best spatial resolution is observed for three active pads.

of the SAT. Throughout this analysis, we refer to these cases as signal-sharing events. Each pad's timing measurement is assumed to carry independent information on the MIP arrival time, enabling a purely timing-based combination of data across the detector plane, following the assumptions made in previous studies [19].

To determine the optimal method for merging timing information from neighboring pads, three combination algorithms were developed and tested. Each method is based on a general weighted-average estimator of the form:

$$t_{\text{comb}}^{\wedge} = \frac{\sum_{k=1}^K (t^k - S(q_{\text{all}}^k)) \cdot w_k}{\sum_{k=1}^K w_k} \quad (6.5)$$

where  $K$  is the number of activated pads,  $t^k$  the measured SAT of pad  $k$ ,  $S(q_{\text{all}}^k)$  the time-walk correction parameterization as a function of the total charge  $q_{\text{all}}^k$ , for each pad individually, as seen in Fig. 11 and  $w_k$  the chosen weighting factor.

The first and simplest approach selects, for each event, the pad that recorded the highest total charge and uses its corrected timing as the event timestamp. In this case, all weights are set to zero except for the pad with the maximum charge, for which  $w_k = 1$ . This method is computationally efficient and serves as a performance baseline.

The second approach extends the idea by weighting each pad's contribution according to its recorded total charge:

$$t_{\text{comb}}^{\wedge} = \frac{\sum_{k=1}^K (t^k - S(q_{\text{all}}^k)) \cdot q_{\text{all}}^k}{\sum_{k=1}^K q_{\text{all}}^k} \quad (6.6)$$

This charge-weighted average improves the representation of shared events, where multiple pads collect significant fractions of the same Cherenkov signal.

Finally, to further optimize the combination, a resolution-weighted approach is introduced. Here, each pad's contribution is weighted by the inverse of its expected timing variance, parameterized as a function of charge:

$$t_{\text{comb}}^{\wedge} = \frac{\sum_{k=1}^K (t^k - S(q_{\text{all}}^k)) \cdot \frac{1}{R^2(q_{\text{all}}^k)}}{\sum_{k=1}^K \frac{1}{R^2(q_{\text{all}}^k)}} \quad (6.7)$$

This formulation gives higher influence to pads with intrinsically better timing resolution. To ensure stability, only pads registering more than 2 pC are considered active and included in the computation.

The comparison of these three algorithms was performed using a structured 2D circular scan across the detector surface. The scan procedure, described earlier, employs a 2D Cartesian grid of sampling points within a circular region that follows the direction of the red arrow in each subplot, with a side length spanning  $\pm 2$  times the outer radius of the hexagon to ensure complete coverage. For each grid point, a circular region of 2 mm radius is defined, and all recorded events within this area undergo the same timing analysis as described previously. This method enables the reconstruction of continuous spatial maps of detector performance. To conclude about the planarity of the board, this scan was performed at different angles.

Using this systematic scan, the combined SAT values obtained from each algorithm were compared over the whole detector area, producing the results shown in Fig. 15. The “maximum-charge” approach (blue curve) performs best near pad centers, while the “resolution-weighted” method (green curve) provides superior response in inter-pad regions, where signals are shared across neighboring channels. The “charge-weighted” approach (orange curve) offers an intermediate behavior between these two extremes.

Overall, the results demonstrate that combining timing data from multiple pads without relying on external spatial information is both feasible and effective. The choice of algorithm may depend

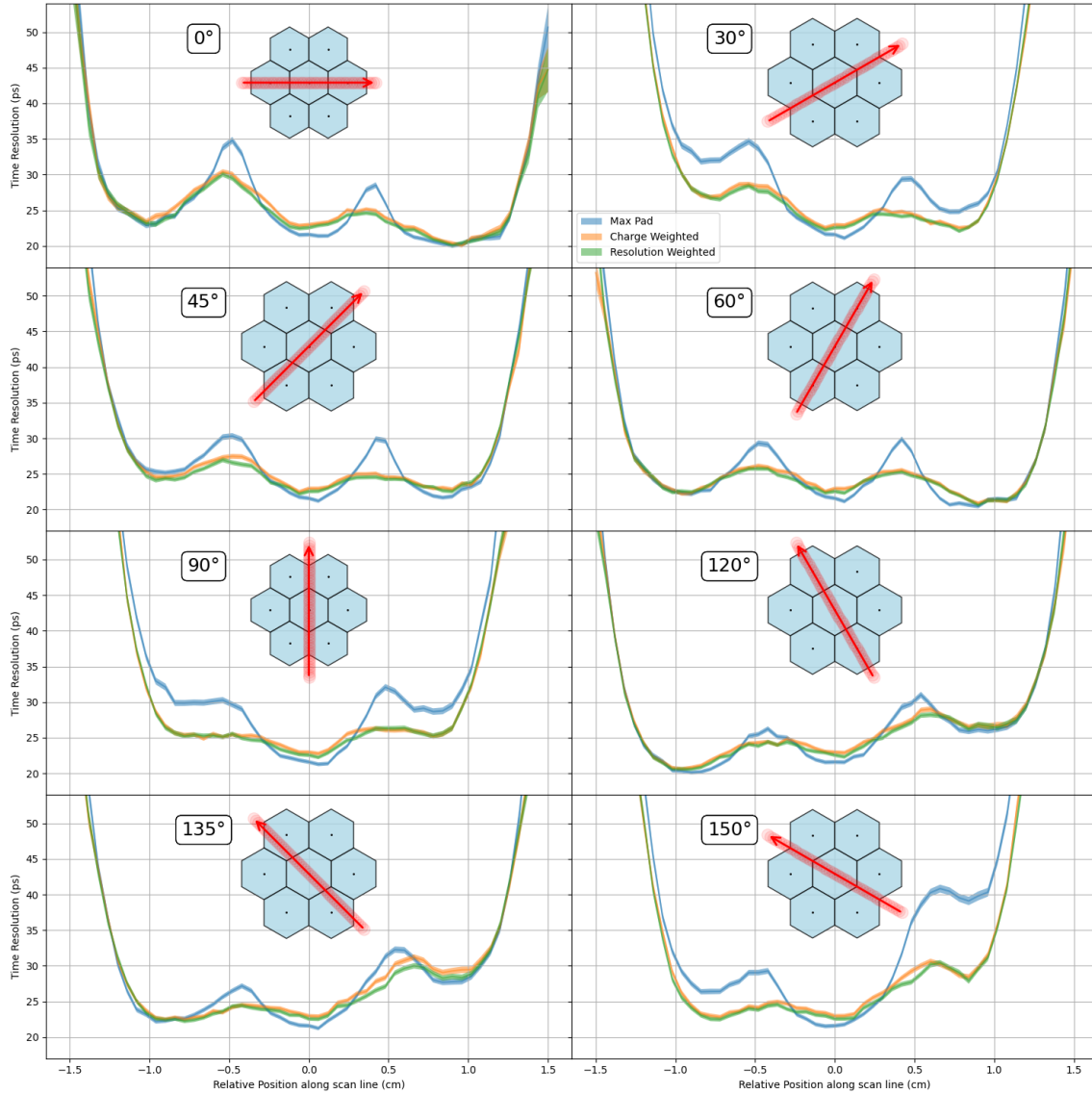


**Figure 15:** Comparison of different weighted average algorithms for combining timing information over the total detector area. With blue, the line corresponds to the maximum pad weighted average, with orange as the charge weighted average, and green as the resolution weighted average. All the plots correspond to eight different observation paths of: 0°, 30°, 45°, 60°, 90°, 120°, 135°, and 150°.

on the experiment's specific performance requirements and computational constraints. In practice, the resolution-weighted combination offers the most balanced and robust approach for accurate time reconstruction across shared regions.

The resulting combined SAT and timing resolution maps are shown in Fig. 16. The SAT map highlights minor systematic effects, such as the small tilt between the photocathode and readout plane, which is possible since the photocathode support is fixed in place with three screws only, while the timing resolution map confirms uniform performance across the detector, achieving an

average resolution better than 35 ps even at pad junctions.

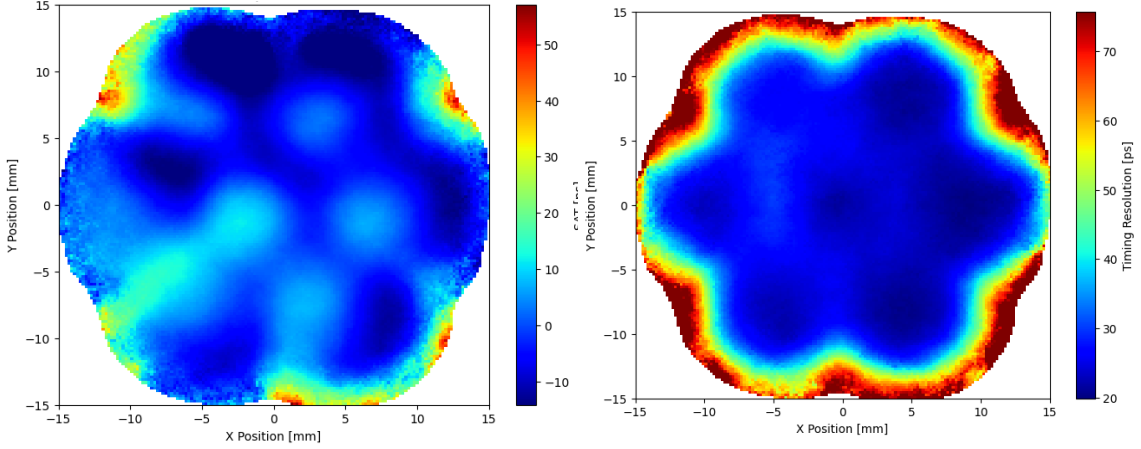


**Figure 16:** Combined corrected SAT and timing resolution 2D circular scan of the whole detector area.

### Focusing in Charge Sharing

The final step of the analysis focuses on the detector’s performance in regions where charge sharing occurs between neighboring pads. This study provides additional validation of the timing combination algorithms discussed above, ensuring their robustness in areas where the Cherenkov cone overlaps multiple readout pads.

To specifically investigate these shared-signal regions, we selected events where the reconstructed hit position lies within the six common corners between the central pad and its adjacent neighbors. In these areas, the Cherenkov cone is typically distributed across an average of three pads, resulting in comparable charge fractions being recorded by multiple channels. For each shared region, the combined timing was computed using the resolution-weighted algorithm described previously, and the resulting SAT distributions were fitted with Gaussian functions to extract the timing resolution. The results, shown in Fig. 17, demonstrate that even in shared regions, a timing resolution better than 28 ps can be achieved, confirming the stability of the combination method across pad boundaries.

To complement the timing performance studies, we also derived the local detection efficiency and event statistics over the entire detector area. The 2D maps were obtained using the same circular scan procedure described previously, where each scan point corresponds to a circular region of 1.5 mm radius centered on the sampling grid position. At each point, the local detection efficiency  $\epsilon(x_i, y_j)$  is defined as:

$$\epsilon(x_i, y_j) = \frac{N_{\text{valid}}(x_i, y_j)}{N_{\text{total}}(x_i, y_j)} \quad (6.8)$$

where  $N_{\text{valid}}(x_i, y_j)$  is the number of events satisfying the detection condition—defined as at least one pad recording a signal with a time difference smaller than 1 ns relative to the reference—

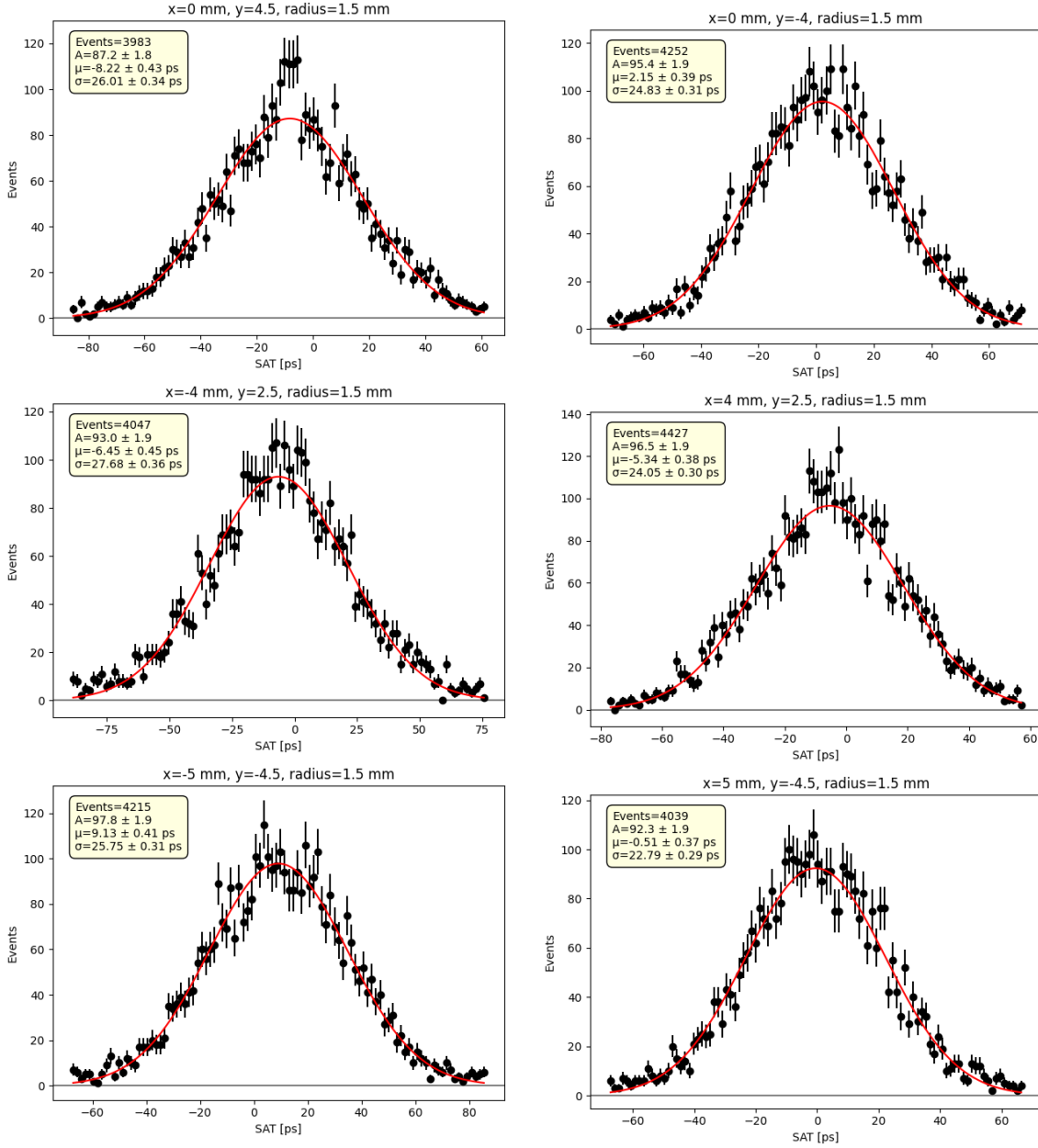


**Figure 17:** Combined corrected timing resolution for the six common corners between the central pad and its neighbors. A consistent performance below 28 ps is observed, validating the robustness of the timing combination method in shared regions.

and  $N_{\text{total}}(x_i, y_j)$  is the total number of events within the corresponding circular region used in the scan.

The resulting maps, shown in Fig. 18, illustrate both the spatial uniformity of the detector response and the event distribution during the scanning run. The high efficiency observed across the active area further supports the uniformity of charge collection and the robustness of the signal reconstruction methods employed.

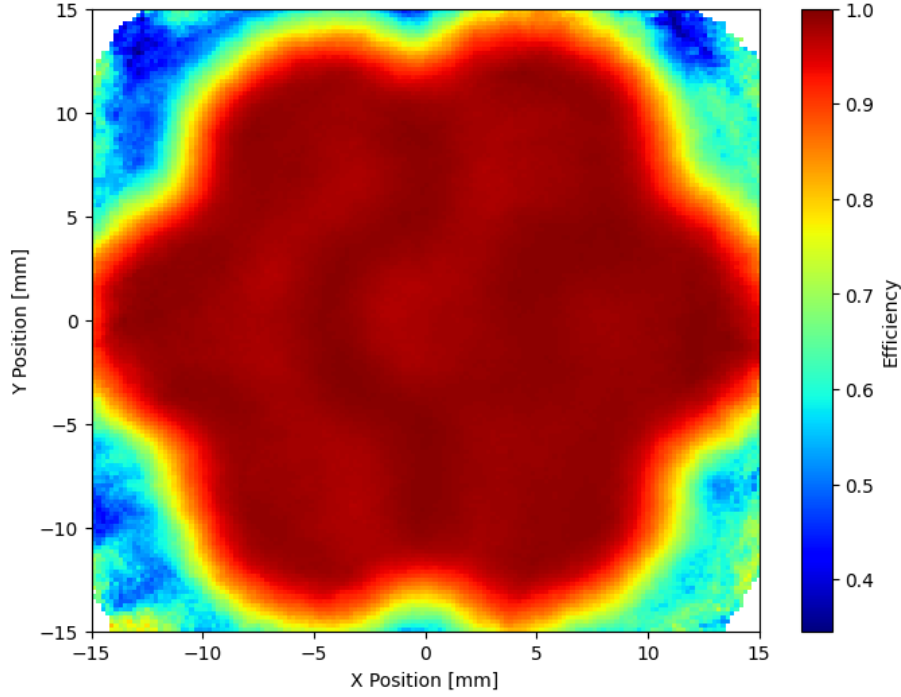


**Figure 18:** Efficiency map over the full detector area.

## 7 Conclusion and Discussion

This work presented a comprehensive characterization of resistive PICOSEC Micromegas detector prototypes, all tested under identical conditions — the same drift gap thickness, field configurations, and photocathode — at the CERN SPS H4 beam line facility. The primary objective was to perform a direct comparison between detectors featuring different resistive layer values and architectural layouts, namely: a simple resistive plane covering the entire readout surface and a capacitive charge-sharing configuration. These studies were motivated by the ENUBET project requirements, which emphasize detector stability under high-rate conditions, efficient spark quenching, and minimal recovery time to guarantee long-term operation [17].

Among all tested prototypes, the configuration employing a  $10\text{ M}\Omega$  resistive layer demonstrated the best overall performance, achieving a timing resolution of  $22.900 \pm 0.002\text{ ps}$  and a spatial resolution of  $1.190 \pm 0.003\text{ mm}$  in both X and Y directions. Charge sharing occurred across an average of three pads, and the detector exhibited uniform timing performance throughout the active area. In regions where signals were shared between neighboring pads, the weighted averaging algorithm — which combines the individual pad SAT using timing-resolution-based weights — recovered a combined timing resolution below  $28\text{ ps}$ .

The comparative analysis across all seven-pad prototypes highlighted the crucial role of resistivity in shaping detector performance. Higher resistivity values effectively localize charge, reducing the amplitude spread of induced signals and improving pad center estimation — a key factor for achieving good spatial resolution. However, the reconstructed position also reflects the intrinsic



resistive charge diffusion, making the apparent hit position subtly dependent on the resistivity value.

The prototype featuring a 200 k $\Omega$  resistive layer displayed a small but statistically consistent shift in reconstructed pad centers relative to their geometric locations. This offset originates from the enhanced charge spread facilitated by the lower resistivity. Nevertheless, the reconstruction algorithm, which identifies the pad with the highest collected charge as the likely impact center, remained robust. This configuration reached a timing resolution of  $31.600 \pm 0.003$  ps and spatial resolutions of  $1.370 \pm 0.004$  mm (X) and  $1.130 \pm 0.003$  mm (Y), with signals typically shared across three pads. When applying the same weighted averaging combination, the resulting timing resolution was approximately 30 ps.

These findings emphasize the importance of mechanical precision — particularly the planarity of the readout board and the parallel alignment of the photocathode. The current support system, relying on peripheral screws to hold the crystal, does not guarantee uniform pressure within the  $\pm 10$   $\mu$ m tolerance required. Deviations larger than 20  $\mu$ m lead to local variations in drift gap thickness and electric field, degrading timing uniformity. Both the 10 M $\Omega$  and 200 k $\Omega$  prototypes exhibited measurable sensitivity to these geometric imperfections, underlining the need for improved mechanical design to ensure full exploitation of the detector’s intrinsic timing capabilities.

In parallel, a capacitive charge-sharing approach was investigated to explore potential improvements in spatial resolution without severely compromising timing precision. Despite also employing a 10 M $\Omega$  resistive layer, this architecture showed a pronounced reduction in signal amplitude, attributed to the presence of intermediate insulating layers in the capacitive stack. Each layer introduces attenuation, resulting in weaker effective signals at the readout pads and, consequently, greater uncertainty in the reconstructed pad centers.

Moreover, the capacitive-sharing geometry — which extends beyond the pad boundaries to cover the entire sensitive region — complicates spatial localization. Particles traversing regions without overlapping pads deposit charge only on the nearest electrode, producing charge clusters that appear displaced from their geometric centers. This broader but weaker charge distribution also affects the observed SAT and timing resolution patterns. Mechanical imperfections further amplified these effects: due to its multi-layered structure, the capacitive prototype exhibited stronger performance degradation in response to PCB deformation and photocathode misalignment.

Despite these challenges, the capacitive-sharing prototype achieved a timing resolution of  $33.300 \pm 0.002$  ps and spatial resolutions of  $0.95 \pm 0.02$  mm (X) and  $1.060 \pm 0.023$  mm (Y). In shared-signal regions, the average timing resolution remained at approximately 31 ps. However, the distinctive behaviors observed in this design — including nonuniform charge distribution and signal attenuation effects — warrant a more detailed study. These phenomena will be thoroughly analyzed in a dedicated future publication, where they will be discussed in conjunction with targeted simulations to better understand the capacitive coupling and charge transport mechanisms.

The insights gained from these studies directly guided the design choices for the next-generation 96-pad detector prototype. The 10 M $\Omega$  resistive layer was selected as the optimal compromise between timing and spatial performance, while the simpler resistive plane configuration was preferred over the capacitive-sharing architecture for its predictable signal behavior and reduced sensitivity to mechanical variations. Overall, the most critical timing and spatial resolution among the different prototypes tested are summarized in Tab.2. Ongoing work focuses on enhancing mechanical stability and ensuring sub-10  $\mu$ m planarity, to fully realize the potential of this resistive Micromegas

technology for precision timing applications within the ENUBET experimental framework, and will be the primary focus of a later publication.

**Table 2:** Summary of performance metrics for resistive PICOSEC Micromegas prototypes.

| Resistive Layer Architecture     | Timing[ $\varnothing 8$ mm](ps) | Spatial X/Y (mm)                | Pad Sharing | Charge Sharing Timing (ps) |
|----------------------------------|---------------------------------|---------------------------------|-------------|----------------------------|
| 10 M $\Omega$ Resistive plane    | $22.9 \pm 0.002$                | $1.19 / 1.19 \pm 0.003$         | 3 pads      | <28                        |
| 200 k $\Omega$ Resistive plane   | $31.6 \pm 0.003$                | $1.37 / 1.13 \pm 0.004 / 0.003$ | 4 pads      | <30                        |
| 10 M $\Omega$ Capacitive sharing | $33.3 \pm 0.002$                | $0.95 / 1.06 \pm 0.02 / 0.023$  | 6 pads      | <31                        |

## Acknowledgments

The authors gratefully acknowledge the support of the French National Research Agency (ANR) through the project “*Development of a PICOSEC-Micromegas detector for ENUBET – PIMENT*” (ANR-21-CE31-0027). The authors also acknowledge the support of the RD51 collaboration in the framework of RD51 common projects. We acknowledge the financial support of the CrossDisciplinary Program on Instrumentation and Detection of CEA, the French Alternative Energies and Atomic Energy Commission. This work was partially supported by the European Union’s Horizon 2020 research and innovation program through the STRONG-2020 project under grant agreement No. 824093.

## References

- [1] E.D.R.R.P. Group, *The 2021 ECFA detector research and development roadmap*, Tech. Rep. CERN-ESU-017, Geneva (2020), DOI.
- [2] H.F.-W. Sadrozinski, A. Seiden and N. Cartiglia, *4d tracking with ultra-fast silicon detectors*, *Reports on Progress in Physics* **81** (2017) 026101.
- [3] R. Santonico and R. Cardarelli, *Development of resistive plate counters*, *Nuclear Instruments and Methods in Physics Research* **187** (1981) 377.
- [4] E. Cerron Zeballos et al., *A new type of resistive plate chamber: The multigap rpc*, *Nuclear Instruments and Methods in Physics Research Section A: Accelerators, Spectrometers, Detectors and Associated Equipment* **374** (1996) 132.
- [5] Y. Giomataris, P. Rebougeard, J. Robert and G. Charpak, *Micromegas: a high-granularity position-sensitive gaseous detector for high particle-flux environments*, *Nuclear Instruments and Methods in Physics Research Section A: Accelerators, Spectrometers, Detectors and Associated Equipment* **376** (1996) 29.
- [6] J. Bortfeldt et al., *Picosec: Charged particle timing at sub-25 picosecond precision with a micromegas based detector*, *Nuclear Instruments and Methods in Physics Research Section A: Accelerators, Spectrometers, Detectors and Associated Equipment* **903** (2018) 317.
- [7] J. Bortfeldt et al., *Modeling the timing characteristics of the picosec micromegas detector*, *Nuclear Instruments and Methods in Physics Research Section A: Accelerators, Spectrometers, Detectors and Associated Equipment* **993** (2021) 165049.
- [8] A. Utrobicic et al., *Single channel picosec micromegas detector with improved time resolution*, 2024.
- [9] A. Utrobicic, et al., *A large area 100-channel picosec micromegas detector with time resolution at the 20 ps level*, *Journal of Instrumentation* **18** (2023) C07012.

- [10] Y. Meng, R. Aleksan, Y. Angelis, J. Bortfeld, F. Brunbauer, M. Brunoldi et al., *Picosec micromegas precise-timing detectors: Development towards large-area and integration*, 2025.
- [11] A. Longhin and F. Terranova, *Enhanced neutrino beams from kaon tagging (enubet)*, 2022.
- [12] C. Aimè, M. Brunoldi, S. Calzaferri, D. Fiorina, C. Riccardi, P. Salvini et al., *Picosec r&d towards muon collider applications*, *Nuclear Instruments and Methods in Physics Research Section A: Accelerators, Spectrometers, Detectors and Associated Equipment* **1082** (2026) 170963.
- [13] D. Janssens, *Resistive electrodes and particle detectors: Modelling and measurements of novel detector structures*, Ph.D. thesis, Vrije U., Brussels, 2024.
- [14] S. Martoiu, H. Muller, A. Tarazona and J. Toledo, *Development of the scalable readout system for micro-pattern gas detectors and other applications*, *Journal of Instrumentation* **8** (2013) C03015.
- [15] J. Bortfeldt, *Development of floating strip micromegas detectors*, Ph.D. thesis, lmu, 2014.
- [16] C. Hoarau et al., *Rf pulse amplifier for cvd-diamond particle detectors*, *Journal of Instrumentation* **16** (2021) T04005.
- [17] A. Kallitsopoulou, *Development of a PICOSEC-Micromegas Detector for ENUBET*, theses, Université Paris-Saclay, July, 2025.
- [18] J. Bortfeldt et al., *Timing performance of a micro-channel-plate photomultiplier tube*, *Nuclear Instruments and Methods in Physics Research Section A: Accelerators, Spectrometers, Detectors and Associated Equipment* **960** (2020) 163592.
- [19] S. Aune, J. Bortfeldt, F. Brunbauer, C. David, D. Desforge, G. Fanourakis et al., *Timing performance of a multi-pad picosec-micromegas detector prototype*, *Nuclear Instruments and Methods in Physics Research Section A: Accelerators, Spectrometers, Detectors and Associated Equipment* **993** (2021) 165076.